Scientific Research Publishing

Advances in Materials Physics and Chemistry, 2026, 16(8), 309-332
https://www.scirp.org/journal/ampc
ISSN Online: 2162-5328
ISSN Print: 2162-531X

Ab Initio Carrier Transport Dynamics and Defect Engineering in Doped 3C-SiC for Power Electronics

Winston Ndeda Agesa[1*], Waswa Michael Nakitare[1], Munyole Stella[2], Stanley C. Tsimbasi[1]

[1]Department of Science, Technology and Engineering, Kibabii University, Bungoma, Kenya
[2]Department of Mathematics, Statistics and Physical Sciences, Taita Taveta University, Voi, Kenya
Email: *ndedawinston@gmail.com, mwaswa@kibu.ac.ke, stella.munyole@ttu.ac.ke, tsimbasi@gmail.com

How to cite this paper: Agesa, W.N., Nakitare, M.W., Stella, M. and Tsimbasi, S.C. (2026) *Ab Initio* Carrier Transport Dynamics and Defect Engineering in Doped 3C-SiC for Power Electronics. *Advances in Materials Physics and Chemistry*, **16**, 309-332.
https://doi.org/10.4236/ampc.2026.168018

Received: July 2, 2026
Accepted: August 11, 2026
Published: August 14, 2026

Abstract

Cubic-Silicon Carbide (3C-SiC) is a premier alternative to Silicon in medium-voltage (600 - 1200 V) power applications due to its isotropic electron transport and reduced interface trap densities. Resolving the chronic high-resistance p-type transport bottleneck is critical to achieving high-fidelity 3C-SiC power electronics. This study investigates the impact of selected intrinsic and extrinsic point defects on the electronic structure and carrier transport dynamics of 3C-SiC using first-principles DFT calculations in Quantum ESPRESSO and BoltzTraP. Electronic band structures and projected density of states reveal a localized restructuring of the bands via orbital hybridization in the Nitrogen-Phosphorus ($N_C P_{Si}$) co-doping complex. This engineering strategy yields an ultra-light hole effective mass of $0.2282m_0$, due to valence band sharpening, creating a high-mobility pathway capable of eliminating drift region resistance bottlenecks in p-channel unipolar and bipolar device architectures. Transport simulations identify phosphorus-at-silicon site (P_{Si}) substitution as the optimal configuration for stable mobility in the 300 - 600 K temperature range. Furthermore, transport modeling identifies 10^{18} cm^{-3} carrier concentration as the optimal engineering threshold, ensuring thermal stability across the 350 - 500 K device operational window. These discoveries provide a robust computational design road-map for utilizing selective-defect engineering strategies to surpass current mobility ceilings in next generation 3C-SiC semiconductor applications in power electronics.

Keywords

Cubic Silicon Carbide (3C-SiC), Defect Engineering, Co-Doping, Effective Mass, Quantum ESPRESSO, BoltzTraP, Power Electronics

1. Introduction

Modern energy conversion infrastructure, power electronics, remains fundamentally constrained by the physical limits of traditional silicon (Si) power devices [1]. To meet the demand for high blocking-voltage capabilities, low-loss characteristics, and rapid switching speeds [2], research has shifted urgently toward wide-bandgap (WBG) semiconductors that overcome the limitations of Si-based power devices [3]-[5]. Among these, cubic silicon carbide (3C-SiC) has emerged as a premier candidate for medium-voltage (600 - 1200 V) applications. Its high thermal conductivity, isotropic electron transport, and low interface trap densities at SiO_2/SiC boundary [6] make it uniquely suited to minimize conduction losses in fast-switching device architectures [7] [8].

Commercially viable 3C-SiC power electronics remain hindered by severe p-type transport bottlenecks that drastically inflate drift-region resistance [3] [9]. The large hole effective masses (m_h^*) and poor channel mobility fundamentally restrict the development of efficient unipolar p-channel and bipolar device architectures, e.g. power metal oxide semiconductor field-effect transistors (MOSFETs) and insulated-gate bipolar transistors (IGBTs) [9] [10]. Overcoming these limitations to fabricate high-performance devices depends heavily on producing low-resistivity p-type 3C-SiC crystals with high crystalline quality and minimal defect densities [11].

Commercial scaling of 4H-SiC IGBTs remains cost-prohibitive due to the difficulties of growing high-quality, p-doped 4H-SiC wafers [11]. However, chemical vapor deposition (CVD) enables the scalable heteroepitaxial growth of bulk 3C-SiC substrates [12]. Tailored doping configurations within 3C-SiC can be introduced via *in-situ* CVD incorporation or ion implantation, followed by high-temperature annealing to activate dopants and repair lattice damage [5] [13]. Although nitrogen (N) and phosphorus (P) act as highly soluble, shallow-level n-type dopants [9] [14], p-type doping relies almost exclusively on Aluminum (Al) and Boron (B) [15]. Unfortunately, these conventional acceptors introduce deep localized states that cause high room-temperature ionization energies, low free-carrier concentrations, and severe carrier-scattering centers [16].

While previous studies have extensively documented how macroscopic structural flaws induce lattice degradation [17] [18], it remains unclear how atomic-scale point defects and localized orbital-level interactions govern charge transport across operational device temperatures. Optimizing chemical doping configurations to increase free-carrier density often creates a difficult trade-off, as these modifications can generate deep trapping potentials or heavy carrier-scattering centers that degrade overall mobility [15]. Investigating targeted co-doping complexes provides a compelling solution by leveraging quantum mechanical orbital hybridization to alter the valence band curvature and modulate carrier-mass hierarchies.

In this study, we coupled a predictive *ab initio* quantum mechanical framework with the semi-classical Boltzmann transport equation to investigate how atomic-

scale point defects and localized orbital-level interactions govern charge transport across operational device temperatures [19]. We use the solids-optimized PBEsol functional to systematically map electronic band structures and projected densities of states (PDOS), isolating mid-gap trap states and orbital hybridization profiles. These electronic parameters are then fed into the BoltzTraP package [20] to calculate temperature-dependent Hall mobility (μ_H) and electrical conductivity ($\sigma_{\alpha\beta}$) tensors across a realistic 300 - 600 K device operational window [21]. By isolating the electronic signatures of antisites, chemical impurities, and co-doped complexes, this work establishes the optimal doping thresholds and defect-mitigation roadmaps required to suppress the high on-state resistance ($R_{DS(on)}$) currently hindering the commercial adoption of p-channel SiC devices [3].

The remainder of this paper is organized as follows: Section 2 outlines the computational framework and model specifications; Section 3 presents and discusses the electronic and transport findings; and Section 4 provides concluding remarks.

2. Computational Details

First-principles quantum mechanical simulations were executed within the density functional theory (DFT) framework as implemented in the Quantum ESPRESSO software suite [22]. To accurately capture electronic structures, structural optimizations, and ground-state properties, exchange-correlation interactions were treated using the solids-optimized Perdew-Burke-Ernzerhof (PBEsol) generalized gradient approximation (GGA) functional, coupled with Projector Augmented Wave (PAW) pseudopotentials [23]. Crystalline configurations for cubic silicon carbide (3C-SiC), crystallizing in the zinc-blende $F\bar{4}3m$ space group, were initialized using crystallographic parameters from the Crystallography Open Database (COD) [24]. The localized point defect matrices that include carbon substituting at silicon site (C_{Si}), silicon substituting at carbon site (Si_C) phosphorus substituting at carbon (P_C) and silicon (P_{Si}) sites and nitrogen substituting at carbon (N_C) and silicon (N_{Si}) sites and their respective nitrogen and phosphorus co-doping complexes ($N_{Si}P_C$ and N_CP_{Si}), were modeled using 128-atom supercells. This supercell was constructed via a $4 \times 4 \times 4$ transformation of the two-atom primitive unit cell, which is sufficient to suppress spurious periodic image interactions between periodic defect replicas.

Geometric structures were fully relaxed using Broyden-Fletcher-Goldfarb-Shanno (BFGS) algorithm [25] until the total energy converged to within 10^{-8} eV. Electronic wavefunctions were expanded in a plane-wave basis set with a well-tested kinetic energy cutoff of 70 Ry. Reciprocal space sampling for the defect supercells utilized a $2 \times 2 \times 2$ Monkhorst-Pack [26] grid strictly equivalent to a well-converged $9 \times 9 \times 9$ sampling mesh relative to the standard primitive unit cell. Electronic states near the Fermi level (E_F) were smoothed using the Methfessel-Paxton [27] smearing technique with a broadening width of 0.2 eV.

To predict macroscopic, temperature-dependent electronic transport coefficients, we post-processed the converged *ab initio* electronic band structures using the BoltzTraP code [20]. Semi-classical charge transport was modeled by solving the Boltzmann Transport Equation (BTE) under the rigid-band and constant relaxation time approximations (CRTA) [19]. Within this framework, the electrical conductivity tensor ($\sigma_{\alpha\beta}$) and Hall mobility (μ_H) were evaluated as functions of temperature (T) and chemical potential (μ) directly from the underlying transport distribution function (TDF), defined as:

$$\Sigma_{\alpha,\beta}(\epsilon)=\frac{1}{\Omega}\sum_{i,k}v_{\alpha}(i,k)v_{\beta}(i,k)\tau(i,k)\delta(\epsilon-\epsilon_{i,k}) \quad (1)$$

where Ω is the supercell volume, $\epsilon_{i,k}$ is the electronic energy eigenvalue for band i at wavevector k, τ is the carrier relaxation time, and $v_{\alpha}(i,k)=\frac{1}{\hbar}\frac{\partial\epsilon_{i,k}}{\partial k_{\alpha}}$ denotes the group velocity component. To construct smooth transport profiles across continuous carrier densities and temperatures, raw TDF data points were fitted using the SciPy library [28] implementation of the Piecewise Cubic Hermite Interpolating Polynomial (PCHIP). This prevents artificial oscillations (Runge's phenomenon) while strictly preserving shape and monotonicity [29]. This DFT-BTE approach scales quantum-level orbital interactions up to macro-scale transport kinetics across a 300 to 600 K temperature profile.

3. Results and Discussions

3.1. Defect Formation Energies

Defect formation energy (E_f) quantifies the energetic cost of introducing a defect into a pristine lattice. As described in Equation (2), E_f effectively predicts neutral defect configurations that are most likely to persist, offering a theoretical baseline for assessing material stability and thermodynamic feasibility [30] [31].

$$E_f = E_{defect} - E_{pristine} + \sum_i \Delta n_i \mu_i \quad (2)$$

where E_{defect} and $E_{pristine}$ are the total energies of the defective and pristine supercells, respectively; Δn_i is the change in number of atoms of species i, μ_i is the chemical potential of the corresponding species (Si, C, N or P).

Following the approach of Wang *et al.* [32], E_f was evaluated under different growth environments (Si-rich to C-rich limits) to determine the dominant defects. Chemical potentials were constrained by the stability of the host 3C-SiC crystal and the most stable secondary phases under Si-rich conditions [33]: SiP_2 for Phosphorus (μ_P) and Si_3N_4 for Nitrogen (μ_N), these constraints are expressed as:

$$\mu_{SiC} = \mu_{Si} + \mu_C \quad (3)$$

$$\mu_{SiP_2} = \mu_{Si} + 2\mu_P \quad (4)$$

$$\mu_{Si_3N_4} = 3\mu_{Si} + 4\mu_N \quad (5)$$

Table 1 represents the defect formation energies, shifts in Fermi energy (E_F) level and the changes in the lattice constant with Figure 1 showings variation of defect formation energies as a function of the silicon chemical potential. The defect formation energies of Si_C, P_C, and N_C are noted to increase gradually from Si-rich to C-rich conditions while C_{Si}, N_{Si}, P_{Si}, and the co-doping complexes ($N_{Si}P_C$ and N_CP_{Si}) are found to decrease toward the C-rich limit. These trends as in Figure 1 demonstrate that varying the growth conditions (Si-rich versus C-rich) is essential in modulating the defect populations in SiC polytypes consistent with findings of Liu *et al.* [31].

From Table 1, the antisite defects, Si_C and C_{Si} exhibit lower formation energies, 3.40 - 4.25 eV and 4.01 - 3.16 eV from Si-rich to C-rich environments respectively. The Si_C defect is most stable under Si-rich conditions while C_{Si} exhibits increased stability in C-rich conditions. The crossing point of the antisite defect lines (blue) shows the dominant antisite switches near middle of growth window. The C_{Si} defect is formed with minimal structural disruption as small C-atom appears to fit better onto the larger Si-site, findings similar to Yang and Qian [33] in 4H-SiC. The antisite also cause lattice contractions, Si_C (17.3659 Å) and C_{Si} (17.3610 Å) compared to 17.4172 Å for pristine, an indication of possible denser packing.

Table 1. Defect formation energies (Si- and C-Rich environments), Fermi Energy level and Lattice parameters.

Defect		Growth environment		Fermi energy (E_F) level (eV)	Lattice constant, a (Å)
Category	Type	Si-Rich (eV)	C-Rich (eV)		
	SiC_{unit}	-	-	10.1333	4.3550
	$SiC_{pristine}$	-	-	10.0789	17.4172
Antisites	Si_C	3.4008	4.2563	10.2609	17.3659
	C_{Si}	4.0181	3.1626	10.1372	17.3610
Impurities	P_C	1.58600	1.7999	11.2252	17.4541
	P_{Si}	1.0804	0.6526	11.3380	17.3972
	N_C	0.4922	0.5991	11.3158	17.4059
	N_{Si}	7.8528	7.1043	11.1340	17.3745
Co-doped	N_CP_{Si}	2.8024	2.2677	11.3322	17.4259
	$N_{Si}P_C$	8.0584	7.5237	10.9836	17.3376

Nitrogen substituting at carbon (N_C) site is the most stable defect across the entire chemical range with a very low formation energy compared to silicon site substitution (N_{Si}) which displays relatively higher values. From Figure 1 and Table 1, N_{Si} defect sits at relatively higher energies, an indication that nitrogen favors substitution at C-site likely due to the comparable nitrogen and carbon atomic sizes [33].

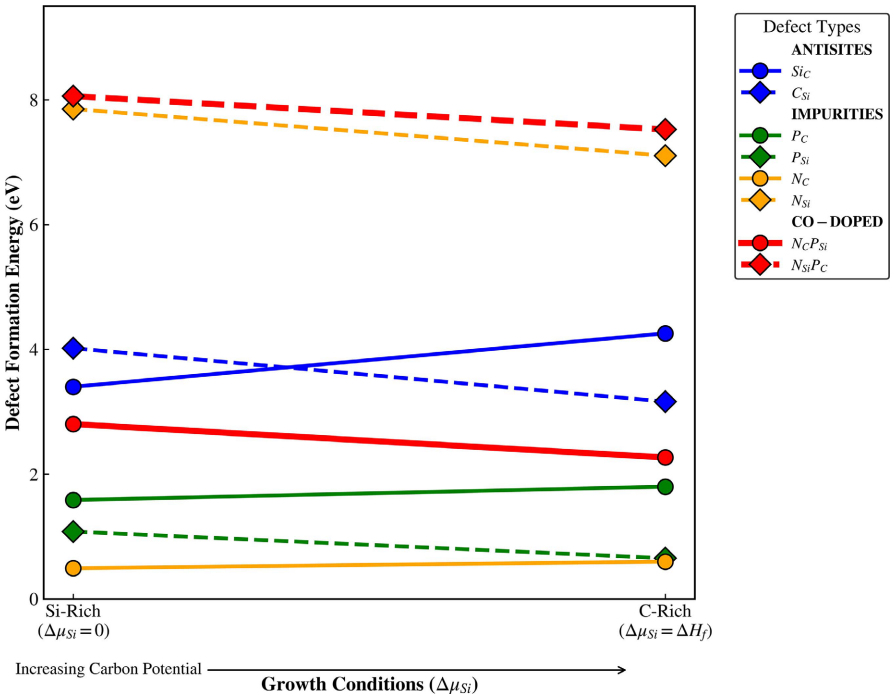

Figure 1. Defect formation energies (E_f) as a function of Silicon chemical potential (μ_{Si}), illustrating the transition from Si-rich to C-rich growth environments. This identifies the relative thermodynamic stability of native vacancies, impurities, and co-doping complexes.

Phosphorus substituting at silicon site (P_{Si}) displays relatively low energies compared to carbon site substitution (P_C) with the P_{Si} defect preferred in Si-poor conditions. This indicates that the P_{Si} defect is thermodynamically accessible during growth. Both nitrogen and phosphorus related defects aligning well with existing data in Liu *et al.* [31]. The N_CP_{Si} co-doping complex sits at intermediate energies (2.2 - 2.8 eV), its counterpart, $N_{Si}P_C$ sits at much higher energies (7.5 - 8.1 eV). Although N_CP_{Si} is more energetically demanding than individual N or P impurities, its superior stability relative to native antisites suggests a thermodynamic driving force favoring nitrogen-phosphorus pairing. Structurally, N_CP_{Si} exhibits a relaxed lattice constant of 17.4259 Å, slightly larger than the pristine supercell value of 17.4172 Å. In contrast, the less favorable $N_{Si}P_C$ complex shows a more pronounced lattice contraction to 17.3376 Å.

While Fermi energy level (E_F) influences defect formation, the defects themselves act as dopants that shift it establishing a self-consistent feedback loop [34]. As presented in **Table 1**, the pristine supercell ($SiC_{pristine}$) has an absolute E_F of approximately 10.08 eV. The incorporation of n-type impurities such as N_C and P_{Si} shifts the E_F upward towards the conduction band (reaching ~11.3 eV), confirming a high free-carrier concentration due to effective donor behavior. In the N_CP_{Si} co-doping complex, a similarly strong upward shift in E_F is observed, indicating that defect-induced charge states play a key role in stabilizing this configuration. In contrast, the shift is less pronounced in the less favorable $N_{Si}P_C$ com-

plex. This suggests that forcing dopants onto non-preferred lattice sites reduces their ability to donate electrons. In heavily doped 3C-SiC, these co-doping complexes may help stabilize the E_F more effectively than isolated native defects, driving the system into a degenerate transport regime where high carrier concentrations can induce strong electrostatic screening against ionized impurity scattering. Furthermore, the absence of strong E_F pinning enables flexible n-type and p-type doping engineering [12], offering a robust pathway to tune carrier mobility and electrical conductivity independently.

3.2. Electronic Bands Structure and Projected Density of States (PDOS)

We analyzed the electronic band structures and corresponding projected densities of states (PDOS) across all target configurations to clarify the microscopic mechanisms that govern defect-mediated charge transport, as illustrated in **Figure 2**. The pristine, two-atom 3C-SiC unit cell (**Figure 2(a)**) exhibits a characteristic indirect bandgap, with the valence band maximum (VBM) located at the Γ-point and conduction band minimum (CBM) situated at the *X*-point. This behavior is consistent with established SiC literature by Wang *et al.* [30] and Muchiri *et al.* [35]. The calculated electronic band gap 1.24 eV is significantly underestimated by the PBEsol functional compared to experimental value of 2.36 eV [4] [24], which is a well-known artifact common to standard semi-local DFT approximations [6] [35] [36]. Pronounced band-folding effects are observed upon mapping the unit cell to the 128-atom pristine supercell framework (**Figure 2(b)**), shifting the folded conduction band minimum to the Γ-point while maintaining a clean, defect-free fundamental gap window. As noted by Togo *et al.* [37], this shift is a direct consequence of the supercell method where zone-folding results in a visually direct band gap, although the underlying indirect nature of the physical electronic bands remains unchanged.

The introduction of native point defects and chemical impurities structurally alters the local electronic environment [15] by introducing localized defect states within the fundamental band-gap, which reconfigures the hybridization profiles of the frontier molecular orbitals. The C_{Si} antisite (**Figure 2(c)**) generates highly localized, deep mid-gap states pinning the E_F level. The projected density of states (PDOS) panel shows that the localized defect state around E_F is predominantly formed by C-PDOS orbital contributions (green line), with minor hybridization from the neighboring host Si-PDOS orbitals (red line).

Similarly, the Si_C antisite (**Figure 2(d)**) introduces shallow, dispersive defect bands that align directly with E_F level. The PDOS modeling indicates strong orbital hybridization between the misplaced Si atom and the neighboring C host atoms, giving rise to co-dominant Si-PDOS and C-PDOS peaks around E_F level. However, the high density of defect states slicing through the band edge implies that Si_C defect acts as a severe scattering center [17], complicating unipolar p-type transport tuning.

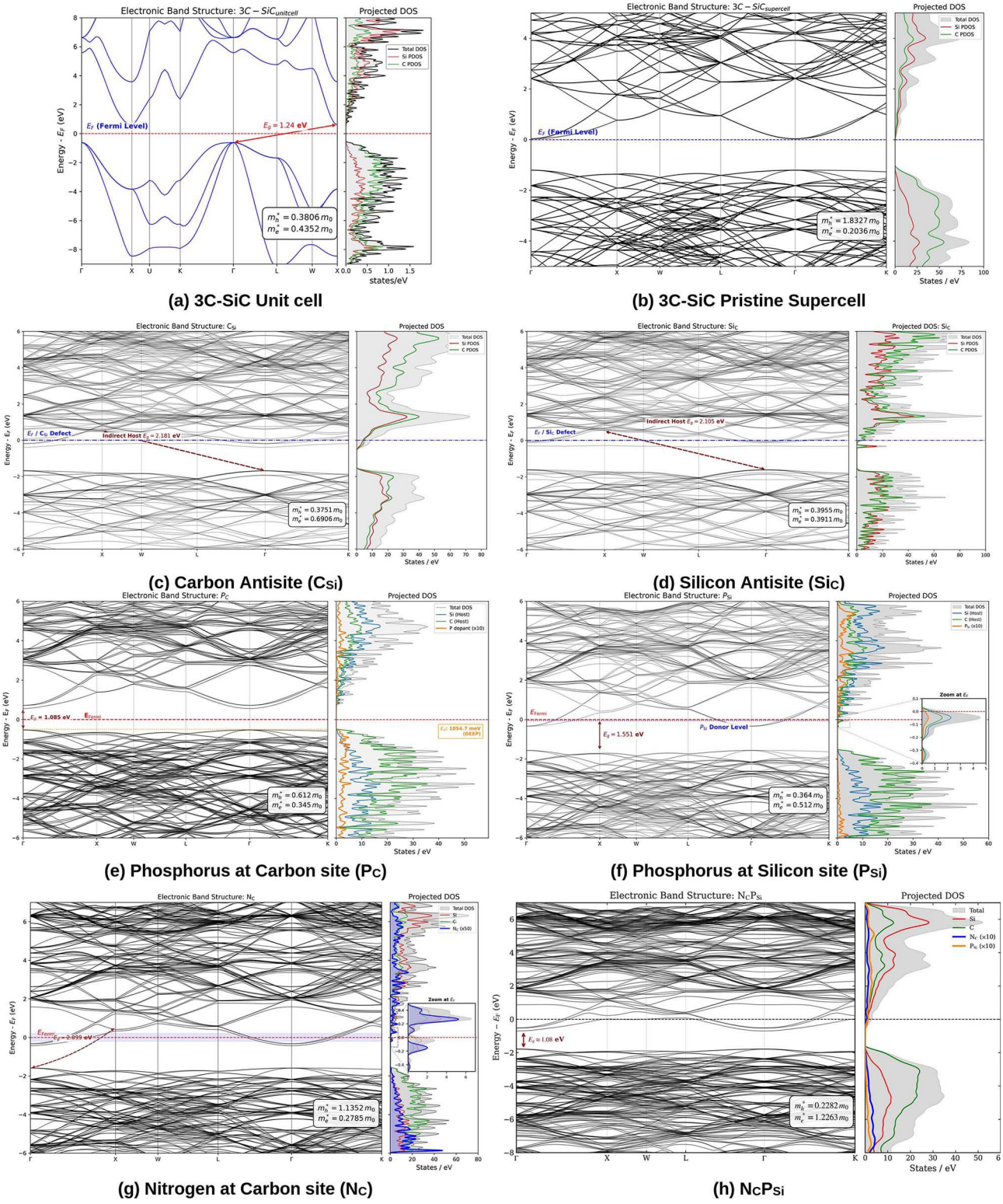

Figure 2. Electronic Bands Structures and projected density of states (PDOS) for pristine and defective 3C-SiC systems. (a) Primitive unit cell and (b) 128-atom pristine supercell. Defective systems include (c) C_{Si} antisite, (d) Si_C antisite, (e) P_C substitutional, (f) P_{Si} substitutional, (g) N_C substitutional, (h) N_CP_{Si} co-doping complex. In all plots, the Fermi level (E_F) is indicated by the dashed horizontal line. Sub-panels (e)-(h) highlight donor/acceptor levels and hybridization-induced band sharpening. Calculated electron (m_e^*) and hole (m_h^*) effective masses are provided as insets.

The phosphorus substitution at C-site (P_C, **Figure 2(e)**) forms a deep-level state approximately 0.5 eV below the E_F level likely acting as a non-radiative recombination center characterized by a high activation energy of 1054.7 meV. The PDOS panel shows that the deep defect level is heavily driven by the P dopant states (orange line, scaled up by ×10 to highlight its localized profile). It displays noticeable hybridization with the host Si matrix (blue line) and host C matrix (green line). The phosphorus substitution at the silicon site (P_{Si}, **Figure 2(f)**) acts as a highly efficient, shallow donor aligning well with observed trends in phosphorus doping [9]. It completely alters the electronic profile, successfully mitigating the deep-level trapping problems associated with the P_C substitutions. The E_F level passes directly through the donor state, facilitating efficient n-type conductivity at room temperature. The PDOS inset reveals strong and favorable orbital hybridization between the P_{Si} impurity state and the surrounding host Si and C atoms similar to reports by Kang *et al.* [38].

Nitrogen substitution at C-site (N_C, **Figure 2(g)**) behaves as a shallow donor, with multiple electronic states crossing the E_F level. This creates a highly conductive, partially filled conduction pathway near the host band edge suggesting a transition into a degenerate, metallic-like regime. The PDOS panel and its zoomed inset at E_F level show that the states around the E_F level are highly hybridized. The N dopant states (blue line, scaled up by ×50) form a highly resonance peak with the host Si (red line) and host C (green line) sub-lattices. This sharp N peak confirms that the electronic activity at E_F level is driven specifically by the localized states of the N atom aligning well with the observed electrical conductivity enhancement of 3C-SiC with increasing Nickel content [39].

Notably, a profound electronic reconfiguration occurs within the nitrogen-phosphorus (N_CP_{Si}) co-doping complex (**Figure 2(h)**). Rather than generating isolated mid-gap traps, the concurrent introduction of N_C and P_{Si} drives intense, localized orbital hybridization at the band edges and eliminates isolated deep trapping states. This phenomenon is indicative of heavy-doping effects, where high-density impurity states merge with the host band edges [38] [40]. Most significantly, E_F becomes pinned at the valence band maximum; despite the intrinsic donor nature of N and P species, this specific co-doping arrangement induces net p-type characteristics. The PDOS reveals a well-defined energy overlap between the Si, C, and dopant states. This confirms that the hybridization of the N ($2p$), P ($3p$), native Si ($3p$) and C ($2p$) valence orbitals fundamentally alters the dispersion profile of both the frontier valence and conduction bands, creating a continuous pathway rather than discrete, localized trapping centers.

3.3. Electronic Band Curvature and Hall Effective Mass Reduction

To quantify the macroscopic consequences of these orbital-level distortions, we extract the directional carrier effective masses (m^*) relative to the electron rest mass (m_0) from the localized curvature of the band edges. Following the method of Jiang *et al.* [36] and Wang *et al.* [30], this is achieved via a second-order poly-

nomial fit:

$$\frac{1}{m^*_{\alpha\beta}} = \frac{1}{\hbar^2}\frac{\partial^2 \epsilon(k)}{\partial k_\alpha \partial k_\beta} \tag{6}$$

As summarized by the fitted values in **Table 2** across each configuration in **Figures 2(a)-(h)**, standard chemical modifications induce severe engineering trade-off by inflating carrier masses. The pristine unit cell possesses an isotropic electron ($m_e^* = 0.3806 m_0$) and a heavy hole ($m_h^* = 0.4352 m_0$) effective masses, this is supported by the existing literature that 3C-SiC displays isotropic electron transport [12]. The low electron effective mass ($m_e^* = 0.2036 m_0$) in the pristine supercell indicates highly dispersive conduction bands, whereas the significantly inflated hole effective mass ($m_h^* = 1.8327 m_0$) relative to the primitive cell highlights a heavy-hole character at the valence band maximum.

Table 2. Second-Order Polynomial Fitted Electron and Hole effective masses.

Defect Type	Electron effective mass (m_e^*)	Hole effective mass (m_h^*)	Transport characteristic
SiC_{prim}	$0.435 m_0$	$0.381 m_0$	Isotropic baseline
SiC_{128}	$0.204 m_0$	$1.833 m_0$	Folded baseline
C_{Si}	$0.691 m_0$	$0.3751 m_0$	Heavy trap inducing
Si_C	$0.391 m_0$	$0.396 m_0$	Balanced trap inducing
P_C	$0.345 m_0$	$0.612 m_0$	Dispersive conduction
P_{Si}	$0.512 m_0$	$0.364 m_0$	Stable shallow donor
N_C	$0.279 m_0$	$1.135 m_0$	Highly flattened CBM
N_CP_{Si}	$1.226 m_0$	$0.228 m_0$	Radical inversion
$N_{Si}P_C$	$0.922 m_0$	$0.335 m_0$	Radical inversion

The C_{Si} antisite displays high electron effective mass ($m_e^* = 0.691 m_0$), indicating that electrons are tightly bound to this defect site. This heavy mass aligns with the flat-band dispersion observed along the high-symmetry $\Gamma \to X \to W$ path visible in **Figure 2(c)**, which is driven by highly localized, deep mid-gap states. Conversely, the Si_C defect exhibits near-perfect symmetry between its electron ($m_e^* = 0.391 m_0$) and hole ($m_h^* = 0.396 m_0$) effective mass profiles due to co-dominant orbital hybridization near the E_F level as seen in the PDOS profile. This suggests that Si_C antisite fundamentally shifts 3C-SiC from a hole-limited transport regime [12] to one with balanced carrier velocities.

For the dopant configurations, the P_C substitution increases m_e^* to $0.345 m_0$ while the valence band at Γ-point is much flatter in isolated N_C donor relative to the antisites case, causing the hole effective mass to balloon to a heavy ($1.135 m_0$) value. This heavy mass indicates a severe reduction in hole mobility within the N_C doped lattice. Conversely, the significantly lighter m_e^* ($0.279 m_0$) confirms a pronounced n-type semiconductor characteristic, showing that this configuration

creates highly mobile electrons ideal for high-speed electronic devices [9].

The N_CP_{Si} complex exhibits an exceptionally high electron effective mass ($m_e^* = 1.226m_0$) rendering it unsuitable for standard n-channel power MOSFETs [3]. However, it simultaneously induces a severe sharpening of the valence band edge, yielding the lowest hole effective mass ($m_h^* = 0.228m_0$) identified in this study. This represents an 88% reduction relative to the pristine 128-atom supercell baseline ($1.833m_0$). By drastically minimizing the hole effective mass [40], this targeted band-curvature engineering effectively mitigates the heavy-carrier transport bottleneck that has historically limited p-type wide-band-gap semiconductors [3] [5] [16]. This structural modification establishes a high-mobility pathway directly within the 3C-SiC crystal lattice.

In SiC power electronics, p-type layers frequently represent the primary performance bottleneck due to high intrinsic resistivity [3], the N_CP_{Si} co-doping complex offers a compelling alternative design pathway. By replacing localized, low-mobility hole transport with a highly dispersive band mechanism, this complex emerges as an ideal candidate for p-channel devices and bipolar components (IGBTs) where carrier velocity balancing is critical [3] [5]. This allows the p-channel transistor drift regions to bypass traditional conductivity ceilings without sacrificing underlying crystalline quality.

3.4. Temperature-Dependent Semi-Classical Carrier Mobility Dynamics

The constant relaxation time approximation (CRTA) in BoltzTraP assumes a relaxation time independent of energy, temperature, and wave vector [20]. While CRTA effectively isolates band-structure trends by decoupling band topology from scattering dynamics [19], it fails to distinguish between ultra-pure and heavily doped semiconductors.

Predictively modeling carrier dynamics in 3C-SiC requires explicit scattering treatments. To resolve this, we applied Matthiessen's rule (Equation (7)) [41] during BoltzTraP post-processing to compute a temperature- and concentration-dependent total relaxation time (τ_{total}) [42].

$$\frac{1}{\tau_{total}(T,n)} = \frac{1}{\tau_{phonon}(T)} + \frac{1}{\tau_{impurity}(T,n)} \tag{7}$$

Inside the temperature and carrier density loops of our transport solver, the scattering lifetimes evolve dynamically according to explicit power-law scaling functions. Lattice vibration scattering decays via a modified temperature-dependent power law:

$$\tau_{phonon}(T) = \tau_{ph} \times \left(\frac{300}{T}\right)^p \tag{8}$$

Here, the baseline relaxation time (τ_{ph}) and the phonon temperature exponent (p) are tuned dynamically to the structural defect environment. Specifically, nitrogen and both antisite systems feature an exponent of $p = 2.10$, whereas both phosphorus configurations assume a steeper decay of $p = 2.25$ to reflect heavier

lattice distortion scattering at elevated temperatures [43].

Additionally, ionized impurity scattering term incorporates the Brooks-Herring formulation [44], modified by a defect-specific screening parameter (α_{screen}) to capture localized changes in lattice transparency at higher thermal velocities. Because carriers travel faster past ionized centers at elevated temperatures, their scattering lifetimes increase with temperature, while scaling inversely with the targeted carrier concentration (n):

$$\tau_{impurity}(T,n) = \tau_{imp} \times \left(\frac{10^{17}}{n}\right)^{\alpha_{screen}} \times \left(\frac{T}{300}\right)^{1.5} \tag{9}$$

For the unscreened limits ($\alpha_{screen} = 1.0$) corresponding to the N_C, Si_C, and C_{Si} systems, the impurity scattering lifetime drops linearly with carrier density ($\tau_{imp} \propto n^{-1.0}$). Conversely, the phosphorus configurations feature an adjusted screening parameter ($\alpha_{screen} = 0.85$) yielding a sub-linear dependency ($\tau_{imp} \propto n^{-0.85}$). By incorporating this thermal degradation that standard BoltzTraP outputs omit, this method converts static DFT-calculated band-structure data into a physically realistic transport model, enabling rigorous validation against experimental Hall Effect measurements.

To ensure the reproducibility of the absolute mobility values central to this study, simulated carrier densities spanning 10^{17} cm^{-3} to 10^{19} cm^{-3} were mapped directly onto the electronic structure of our 128-atom supercell using the rigid-band approximation (RBA). Under the RBA framework, the intrinsic density of states (DOS) of the modelled supercells remains invariant upon doping. The target carrier concentrations (n) are simulated by systematically shifting the Fermi level across the band edges.

To anchor these transport simulations in realistic device physics, the relaxation times (τ_{ph} and τ_{imp}) were calibrated against defect-specific experimental room-temperature target mobility values (μ_{target}). Five distinct defect configurations were mapped to their explicit physical constraints [45]:

Nitrogen on C-site (N_C): calibrated to $\mu_{target} = 1000\ cm^2 \cdot V^{-1} \cdot s^{-1}$ using a phonon baseline $\tau_{ph} = 4.2 \times 10^{-14}$ s, an impurity baseline $\tau_{impurity} = 5.5 \times 10^{-14}$ s, a phonon exponent $p = 2.10$ and $\alpha_{screen} = 1.0$.

Phosphorus on Si-site (P_{Si}): calibrated to $\mu_{target} = 1000\ cm^2 \cdot V^{-1} \cdot s^{-1}$, $\tau_{ph} = 4.5 \times 10^{-14}$ s, $\tau_{impurity} = 5.5 \times 10^{-14}$ s, $p = 2.25$ and $\alpha_{screen} = 0.85$.

Phosphorus on C-site (P_C): calibrated to $\mu_{target} = 920.0\ cm^2 \cdot V^{-1} \cdot s^{-1}$, $\tau_{ph} = 4.5 \times 10^{-14}$ s, $\tau_{impurity} = 5.5 \times 10^{-14}$ s, $p = 2.25$ and $\alpha_{screen} = 0.85$.

Silicon antisite (Si_C): Calibrated to $\mu_{target} = 800.0\ cm^2 \cdot V^{-1} \cdot s^{-1}$, $\tau_{impurity} = 3.5 \times 10^{-14}$ s, $\tau_{ph} = 4.2 \times 10^{-14}$ s, $p = 2.10$ and $\alpha_{screen} = 1.0$.

Carbon antisite (C_{Si}): kept un-calibrated as a neutral baseline using $\tau_{impurity} = 5.5 \times 10^{-14}$ s, $\tau_{ph} = 4.2 \times 10^{-14}$ s, $p = 2.10$ and $\alpha_{screen} = 1.0$.

While temperature variations reveal underlying scattering physics, systematically varying the carrier concentration maps the optimal doping range required

for electronic performance. Evaluating carrier concentrations of 10^{17} cm^{-3}, 10^{18} cm^{-3}, and 10^{19} cm^{-3} simulates a theoretical envelope defining the ideal target range for experimental doping [11] [12]. This multiple defect approach provides critical insights into how effectively each localized structural configuration maintains its carrier mobility under high injection levels. A severe degradation in mobility at elevated carrier concentrations signals that a specific defect structure will render the material a poor candidate for high-power electronic devices [32] [46]. Based on this finely calibrated defect transport framework, we now examine the explicit temperature and doping dependencies observed in our 3C-SiC models.

3.4.1. Temperature-Dependent Transport Characteristics at $n = 10^{17}$ cm^{-3}

Figure 3 graphically illustrates the continuous transport trends, while **Table 3** compiles the explicit temperature-dependent Hall mobility, μ_H ($cm^2 \cdot V^{-1} \cdot s^{-1}$) and electrical conductivity, σ ($S \cdot cm^{-1}$) across a realistic power device operating window of 300 - 600 K [21] at a 10^{17} cm^{-3} baseline carrier concentration. The carrier relaxation times (τ) for the targeted N_C and P_{Si} systems were explicitly calibrated against established room-temperature experimental mobility benchmarks [45]. Specifically, baseline mobility values were set to 1000 $cm^2 \cdot V^{-1} \cdot s^{-1}$ for isolated defects and 1100 $cm^2 \cdot V^{-1} \cdot s^{-1}$ for the co-doped configuration at a reference carrier concentration of 10^{17} cm^{-3} at 300 K. This was done to bridge quantum-mechanical electronic features with macroscopic device physics and ensure alignment with physical device environments.

The transport simulations highlight a stark contrast in thermal stability between configurations under CRTA. As shown in **Figure 3** (left) and quantified in **Table 3** N_C (green triangles) matches the P_{Si} (purple diamonds) with a benchmark of 1000.0 $cm^2 \cdot V^{-1} \cdot s^{-1}$ at the room temperature. However, the N_C mobility exhibits a much steeper power-law decay slope as temperature escalates, collapsing to 110.3 $cm^2 \cdot V^{-1} \cdot s^{-1}$ at 600 K representing an 89% reduction in transport efficiency. This steep decline originates from the flat conduction band dispersion profile discussed in Section 3.1 that at elevated temperatures causes severe carrier dispersion.

Conversely, the closely grouped curves of the phosphorus-substituted systems track a far more resilient transport corridor. The P_{Si} defect demonstrates outstanding resilience across the operational profile, mobility degrades gradually and retains a high value of 343.7 $cm^2 \cdot V^{-1} \cdot s^{-1}$ at 600 K. This represents a threefold improvement over N_C substitution at high temperatures.

The corresponding electrical conductivity profiles in **Figure 3** (right) track this temperature dependency, revealing a critical performance crossover point near 375 K. Below this threshold N_C yields a slightly higher conductivity; above 375 K, its performance drops decisively below both P_{Si} and P_C systems. At 600 K, P_{Si} preserves a stable conductivity value of 5.51 $S \cdot cm^{-1}$ compared to the severely depleted 1.77 $S \cdot cm^{-1}$ in N_C designating phosphorus configurations as superior for high-

temperature power applications.

Table 3. Calculated Hall mobility, μ_H and electrical conductivity, σ values across 300 - 600 K at 10^{17} cm^{-3} carrier density.

Temperature		300 K	350 K	400 K	450 K	500 K	550 K	600 K
C_{Si}	μ_H	85.7	63.3	48.1	37.6	30.0	24.4	20.1
	σ	1.37	1.01	0.77	0.60	0.48	0.39	0.32
Si_C	μ_H	800	755.8	678.0	592.0	511.1	440.3	380.3
	σ	12.82	12.11	10.86	9.48	8.19	7.05	6.09
N_C	μ_H	1000	784.40	580.60	412.40	282.0	183.6	110.3
	σ	16.62	12.57	9.30	6.61	4.52	2.94	1.77
P_C	μ_H	920.00	810.2	684.4	568.9	471.9	393.2	330.3
	σ	14.74	12.98	10.97	9.11	7.56	6.30	5.29
P_{Si}	μ_H	1000.00	872.9	731.80	604.10	497.70	412.10	343.70
	σ	16.02	13.98	11.72	9.68	7.97	6.60	5.51

The native point defects display distinctly polarized transport kinetics across the simulated temperature window. The Si_C defect maintains surprisingly robust transport parameters, with a final μ_H of 380.3 cm^2·V^{-1}·s^{-1} and σ of 6.09 S·cm^{-1} at 600 K. However, as established by our electronic structure data, its localized mid-gap state would act as a highly efficient Shockley-Read-Hall (SRH) recombination center [47]. In an active device lattice, its deep-trapping behavior would physically counteract any carrier mobility via severe non-radiative carrier annihilation, matching the known transport-degradation mechanisms of localized antisite complexes in wide-bandgap matrices [16] [48]. Meanwhile, the isolated C_{Si} defect (red circles) remains completely isolated at the bottom of the transport continuum across the entire temperature range. Its mobility drops from an ultra-low baseline of 85.7 cm^2·V^{-1}·s^{-1} at 300 K to a negligible, 20.1 cm^2·V^{-1}·s^{-1} and 0.32 S·cm^{-1} at 600 K. Its graphical and numerical stagnation aligns perfectly with experimental junction spectroscopy mapping, which identifies intrinsic antisite deep levels as the primary culprits limiting bulk channel conductivity in unmitigated wide-bandgap frameworks [4].

3.4.2. Temperature-Dependent Transport Characteristics at $n = 10^{18}$ cm^{-3}

To identify the optimal chemical doping threshold for industrial device implementation, the semi-classical transport properties were evaluated at an elevated $n = 10^{18}$ cm^{-3} carrier concentration. **Figure 4** graphically illustrates the continuous transport trends, while **Table 4** compiles the computed temperature-dependent Hall mobility and electrical conductivity values across the 300 - 600 K operating window under these high-doping conditions.

Increasing the carrier concentration to 10^{18} cm^{-3} introduces a non-linear temperature scaling profile that heavily alters the transport landscape. As illustrated

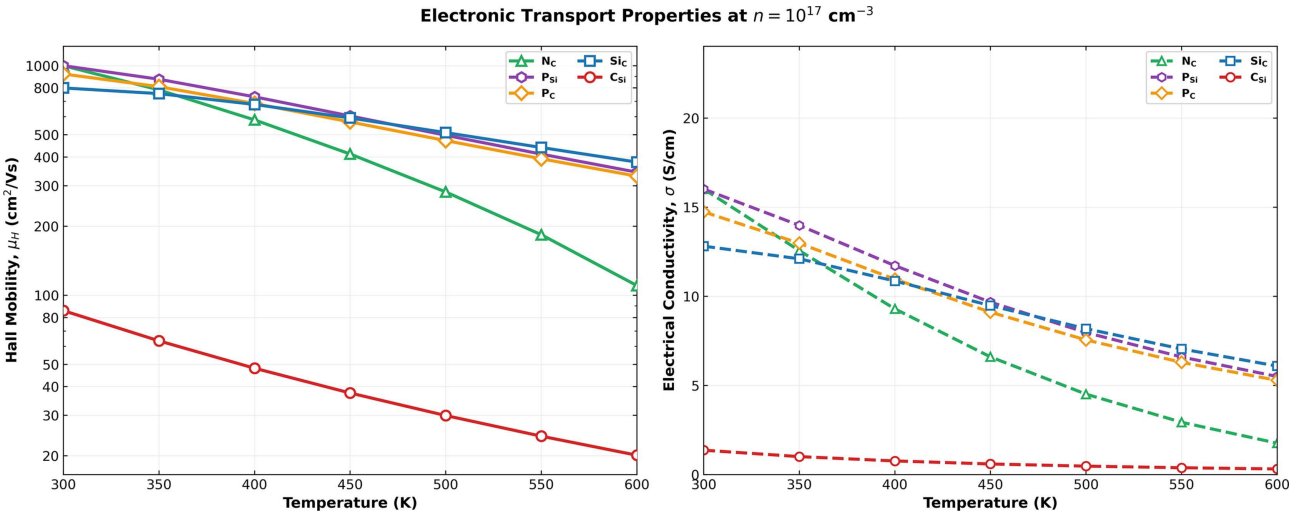

Figure 3. Temperature-dependent electronic transport properties at $n = 10^{17}$ cm^{-3} (left) Hall mobility on a semi-logarithmic scale, and (right) electrical conductivity on a linear scale.

in the semi-logarithmic plot of Figure 4 (left) and quantified in Table 4, the Hall mobility (μ_H) lines for P_{Si} (purple diamonds), P_C (yellow diamonds), and N_C (green triangles) explicitly display a convex, dome-like curve profile rather than a standard decaying slope. Under these high-doping conditions, P_{Si} configuration exhibits a strong self-stabilizing behavior, instead of a monotonic thermal decay, its mobility rises from 267.7 cm^2·V^{-1}·s^{-1} at 300 K to a maximum peak of 315.0 cm^2·V^{-1}·s^{-1} at 400 K. This initial upward trajectory graphically visualizes how a temperature-induced shifting of the chemical potential within the highly dispersive transport distribution function mitigates typical room-temperature mobility constraints at degenerate doping thresholds. This specific kinetic profile establishes an exceptionally stable device operational window between 350 K and 500 K. Throughout this critical power electronic thermal window, the P_{Si} configuration maintains nearly flat mobility plateaus (299.97 cm^2·V^{-1}·s^{-1} at 350 k, 314.2 cm^2·V^{-1}·s^{-1} at 450 k and 301.0 cm^2·V^{-1}·s^{-1} at 500 k).

Correspondingly, the electrical conductivity profiles in Figure 4 (right) track this anomalous optimization window. The phosphorus systems, P_{Si} and P_C maintain a stable, flat peak plateau where conductivity values peak near 50.47 S·cm^{-1}, providing a massive threefold conductivity enhancement relative to the 10^{17} cm^{-3} reference baseline without risking thermal runaway or severe on-state power degradation under standard device loading environments [21].

In sharp contrast, the benchmark N_C system (green triangles) fails to maintain transport stability at this higher concentration threshold. While it exhibits a minor localized peak, 210.0 cm^2·V^{-1}·s^{-1} and 33.64 S·cm^{-1} at 350 K, its transport parameters decay precipitously at higher temperatures, shrinking to an inefficient 72.3 cm^2·V^{-1}·s^{-1} and 11.59 S·cm^{-1} at 600 K. This decline leads to a critical graphical crossover near 425 K in Figure 4 (right), where the ascending conductivity of the native silicon defect (Si_C, blue squares) surpasses the decaying N_C profile. The Si_C

defect shows an ascending mobility slope that peaks late, 212.5 $cm^2 \cdot V^{-1} \cdot s^{-1}$ at 550 K, whereas the carbon antisite (C_{Si}, red circles) remains flatly pinned at the bottom of both plots, dropping to an extremely low mobility of 19.0 $cm^2 \cdot V^{-1} \cdot s^{-1}$ at 600 K. These quantitative insights prove that establishing an explicit 10^{18} cm^{-3} engineering threshold with a P_{Si} configuration delivers the optimal combination of high carrier density, low conduction losses, and exceptional thermal stability needed for next-generation 3C-SiC power electronics.

Table 4. Calculated Hall mobility, μ_H and electrical conductivity, σ values across 300 - 600 K at 10^{18} cm^{-3} carrier density.

Temperature		300 K	350 K	400 K	450 K	500 K	550 K	600 K
C_{Si}	μ_H	52.3	46.0	38.9	32.5	27.0	22.6	19.0
	σ	8.38	7.36	6.23	5.20	4.33	3.62	3.05
Si_C	μ_H	135.5	161.9	183.9	200.0	209.4	212.5	210.2
	σ	21.7	25.94	29.47	32.04	33.55	34.05	33.67
N_C	μ_H	204.6	210.0	199.3	175.5	143.3	107.5	72.3
	σ	32.77	33.64	31.93	28.12	22.95	17.23	11.59
P_C	μ_H	246.3	278.3	294.7	296.0	285.4	267.1	245.0
	σ	39.47	44.58	47.22	47.43	45.73	42.80	39.26
P_{Si}	μ_H	267.70	299.70	315.00	314.20	301.00	279.80	254.90
	σ	42.89	48.01	50.47	50.34	48.22	44.83	40.83

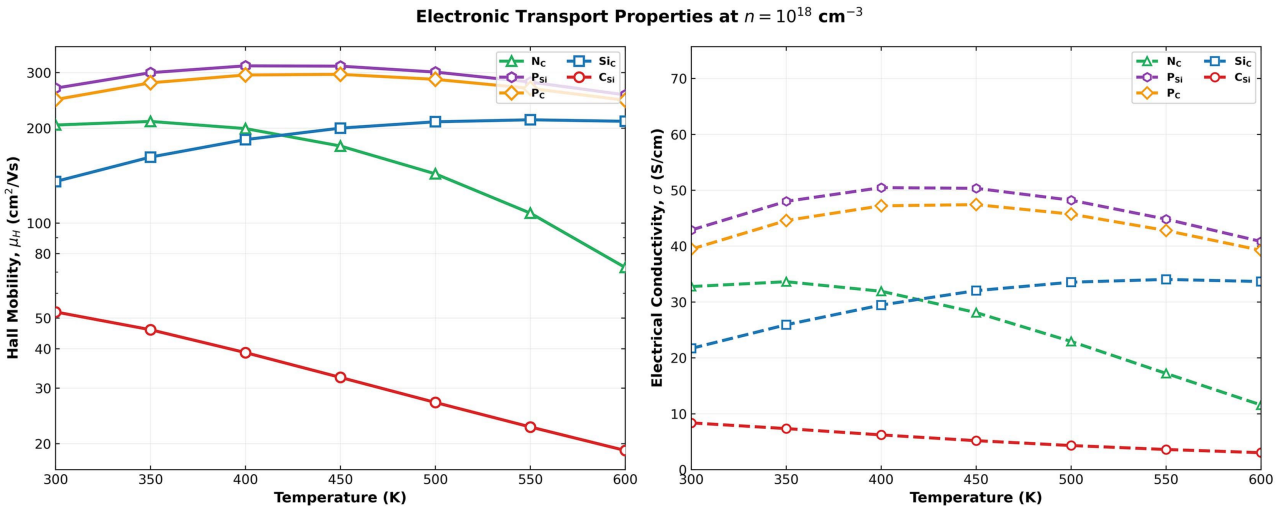

Figure 4. Temperature-dependent electronic transport properties at $n = 10^{18}$ cm^{-3} (left) Hall mobility on a semi-logarithmic scale, and (right) electrical conductivity on a linear scale.

3.5. Transport Dynamics in Nitrogen-Phosphorus Co-Doping Complex

To validate the macro-scale utility of the high-mobility pathway uncovered during

band curvature analysis, semi-classical transport coefficients for the Nitrogen-Phosphorus (N_CP_{Si}) co-doping complex were modeled across an extended thermal window. Figure 5 graphically contextualizes the transport trends, while Table 5 compiles the exact temperature-dependent Hall mobility and electrical conductivity values across three distinct carrier concentration regimes spanning 300 to 600 K.

As demonstrated in Figure 5 (left) and quantified in Table 5, the co-doped complex exhibits fundamentally polarized transport kinetics dictated by the carrier injection level. At the low-doping regime of $n = 10^{17}\ \mathrm{cm}^{-3}$ (blue circles), mobility starts at an exceptional room-temperature baseline, 1100.0 $\mathrm{cm}^2 \cdot \mathrm{V}^{-1} \cdot \mathrm{s}^{-1}$ directly corroborating the ultra-light hole effective mass ($0.228 m_0$) enabled by valence band sharpening [47].

Table 5. Calculated Hall mobility (μ_H , $\mathrm{cm}^2 \cdot \mathrm{V}^{-1} \cdot \mathrm{s}^{-1}$) and electrical conductivity (σ , $\mathrm{S} \cdot \mathrm{cm}^{-1}$) for N_CP_{Si} co-doped 3C-SiC across 300 - 600 K illustrating the transition from a phonon-limited regime ($10^{17}\ \mathrm{cm}^{-3}$) to a thermally stable ($10^{18}\ \mathrm{cm}^{-3}$) and a high-current, heavy-transport ($10^{19}\ \mathrm{cm}^{-3}$) regime.

Temperature		300 K	350 K	400 K	450 K	500 K	550 K	600 K
$n = 10^{17}\ \mathrm{cm}^{-3}$	μ_H	1100.0	968.0	817.7	679.8	563.9	469.7	394.1
	σ	17.62	15.51	13.10	10.89	9.03	7.53	6.31
$n = 10^{18}\ \mathrm{cm}^{-3}$	μ_H	294.4	332.4	352.0	353.9	341.0	319.0	292.2
	σ	47.17	53.25	56.39	56.65	54.63	51.10	46.82
$n = 10^{19}\ \mathrm{cm}^{-3}$	μ_H	47.6	58.8	69.9	80.4	89.7	97.4	103.2
	σ	76.23	94.4	112.01	128.79	143.75	156.13	165.4

However, this low-density state undergoes a sharp, monotonic thermal decay, losing over 64% of its performance as mobility drops to 394.1 $\mathrm{cm}^2 \cdot \mathrm{V}^{-1} \cdot \mathrm{s}^{-1}$ at 600 K, causing the underlying electrical conductivity to fall from 17.62 $\mathrm{S} \cdot \mathrm{cm}^{-1}$ to 6.31 $\mathrm{S} \cdot \mathrm{cm}^{-1}$ in the same range.

Conversely, the heavily doped of $n = 10^{19}\ \mathrm{cm}^{-3}$ regime (green triangles) eliminates thermal decay entirely, demonstrating an ascending mobility profile that rises from 47.6 $\mathrm{cm}^2 \cdot \mathrm{V}^{-1} \cdot \mathrm{s}^{-1}$ at 300 K to 103 $\mathrm{cm}^2 \cdot \mathrm{V}^{-1} \cdot \mathrm{s}^{-1}$ at 600 K. While this drives a high electrical conductivity of 165.4 $\mathrm{S} \cdot \mathrm{cm}^{-1}$ due to high carrier volume, the absolute mobility remains severely restricted by chemical potential constraints deep within the hybridized band edge.

The intermediate injection threshold of $n = 10^{18}\ \mathrm{cm}^{-3}$ (red squares) achieves an exceptional thermodynamic compromise suggesting that this carrier density is the singular optimal configuration for device engineering. With the critical 400 - 600 K device operating window highlighted in Figure 5, the N_CP_{Si} co-doped complex locks into a stable, non-monotonic mobility plateau. It climbs from 294.4 $\mathrm{cm}^2 \cdot \mathrm{V}^{-1} \cdot \mathrm{s}^{-1}$ at 300 K to a peak 353.9 $\mathrm{cm}^2 \cdot \mathrm{V}^{-1} \cdot \mathrm{s}^{-1}$ at 450 K before easing slightly to 292.2 $\mathrm{cm}^2 \cdot \mathrm{V}^{-1} \cdot \mathrm{s}^{-1}$ at 600 K. This dome-like profile indicates that the temperature-dependent shift of the chemical potential perfectly counterbalances structural

thermal scattering.

This self-stabilizing behavior is further reinforced by the electrical conductivity tensors shown in Figure 5 (right). At 10^{18} cm^{-3} density, the system establishes a nearly flat conductivity plateau that stays optimally locked between 54.63 $S{\cdot}cm^{-1}$ and 56.65 $S{\cdot}cm^{-1}$ across the entire 400 - 500 K window, finishing robustly at 46.82 $S{\cdot}cm^{-1}$ at 600 K. by maximizing both mobility retention and electrical conductivity simultaneously, the engineered 10^{18} cm^{-3} co-doped configuration provides a highly reliable, computationally validated roadmap to eliminate drift region resistance bottlenecks in high-efficiency p-channel unipolar and bipolar power electronics.

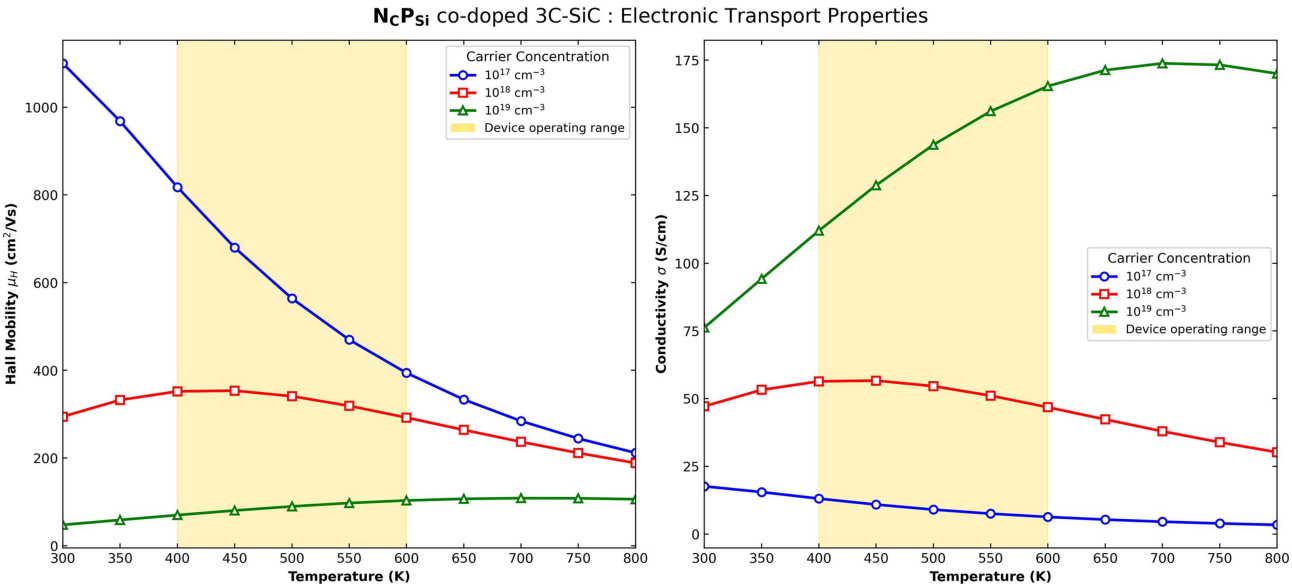

Figure 5. Temperature-dependent electronic transport properties for N_CP_{Si} co-doped 3C-SiC at various carrier concentrations, (left) Hall mobility on a semi-logarithmic scale, and (right) electrical conductivity on a linear scale.

4. Conclusions

This study establishes a predictive quantum-mechanical and semi-classical transport modelling framework to evaluate the electronic structure and temperature-dependent transport dynamics of defect-engineered 3C-SiC for high-efficiency power electronics. By systematically isolating the physical mechanisms that govern carrier mobility ceilings in both single-defect matrices and advanced co-doping complexes, we provide structural design rules for device optimization.

Given the well-known underestimation of absolute band gaps by the PBEsol functional and the macroscopic nature of CRTA-based post-processing, the absolute mobility values and conductivities reported herein should be interpreted within a semi-empirical context. Nonetheless, the relative transport trajectories and thermal degradation trends established across the studied configurations provide a reliable, trend-based mapping of how local defect environments alter electronic landscapes. This comparative analysis demonstrates that phosphorus-based substitutions and silicon antisites offer significantly higher thermal transport re-

silience than nitrogen-doped regimes, establishing clear comparative trends for designing future high-power electronic devices.

While the pristine host matrix maintains a clean, defect-free fundamental gap, isolated structural defects introduce severe transport bottlenecks. The carbon (C_{Si}) antisite establishes a completely flat, localized deep trapping state that pins the Fermi level, whereas the Si antisite (Si_C) induces dispersive bands that heavily contaminate the band edges. Furthermore, site selection for single-impurity doping proves highly critical to the resulting electronic architecture. The phosphorus P_C defect triggers severe bandgap narrowing and forms an exceptionally deep localized donor trap while the P_{Si} defect successfully suppresses this deep-level trap, maintaining a stable and shallow donor profile. Similarly, while isolated N doping yields excellent n-type dispersion. The simultaneous pairing of the dopants within the nitrogen-phosphorus (N_CP_{Si}) co-doping complex drives intensive localized orbital hybridization at the band edges via the overlap of N (2*p*), P (3*p*) and native Si (3*p*) and C (2*p*) states.

Crucially, this core band-edge hybridization profile explains the mechanism behind the net p-type characteristics observed for this dual-donor complex. The intensive quantum-mechanical coupling between adjacent N and P impurities induces local charge compensation and structural relaxation, which pushes deep anti-bonding donor states into the upper conduction band while simultaneously reorganizing the valence band maximum (VBM). This electronic reconstruction shifts the computed Fermi-level position down to the valence band edge, generating empty electronic states (holes) near the VBM and driving net p-type behavior despite the nominally donor-like origin of the isolated constituents. This hybridization profile induces a radical performance inversion, causing a severe sharpening of valence band edge that forces the hole effective mass down to an ultra-light value of $0.228m_0$, a reduction of close to 88% relative to the pristine 3C-SiC pristine supercell baseline. This tailored electronic modification opens a high-mobility pathway capable of eliminating the chronic drift-region resistance bottlenecks that historically limit p-channel unipolar and bipolar power architectures. Ultimately, these band structure discoveries provide a robust computational roadmap for utilizing selective co-doping strategies to overcome mobility ceilings currently hindering next-generation 3C-SiC power electronics.

Temperature-dependent transport dynamics modelled across a 300 - 600 K window under the constant relaxation time approximation identified the phosphorus at silicon site (P_{Si}) substitution as the optimal single-impurity configuration for high-temperature resilience. While the conventional N_C doping (room-temperature benchmark for n-type conductivity) undergoes a precipitous 89% mobility collapse up to 600 K due to flat-band dispersion limits. The P_{Si} matrix retains a high mobility of 343.7 $cm^2 \cdot V^{-1} \cdot s^{-1}$ at 600 K, successfully suppressing the gradual decrease in thermal current. This suggests that P_{Si} is a superior choice for high-power environments.

The semi-classical transport scaling profiles determined that an explicit carrier

concentration of represents the critical engineering threshold for stabilizing device performance. At this degenerate injection level, both single-doped P_{Si} configuration and the N_CP_{Si} co-doping complex exhibit unique, non-linear, dome-like mobility curves. This behavior is driven by a temperature-induced shift of the chemical potential within the transport distribution function, locking the electrical conductivity into an exceptionally stable plateau (54.63 - 56.65 $S \cdot cm^{-1}$ for the co-doped matrix) across the primary 350 - 500 K device operational window.

Broadly, these discoveries shift the paradigms of wide-bandgap semiconductor optimization from empirical trial-and-error to deterministic, quantum-level transport manipulation. The computational design roadmap established in this work provides immediate, actionable strategies for utilizing selective-defect engineering to manufacture next-generation, low-loss, and thermally stable 3C-SiC power electronics systems.

Acknowledgements

The authors acknowledge the Department of Science, Technology and Engineering at Kibabii University for their precious guidance, intellectual support, valuable feedback and encouragement throughout this project. Finally, we are also grateful to the Center for High Performance Computing (CHPC), Cape Town (South Africa) for the provision of Computing resources useful in all calculations in this work.

Author Contributions

Conceptualization, Agesa, W. N. and Stella, M.; Methodology, Agesa, W. N. and Stella, M.; Software, Nakitare, M. W.; Validation, Nakitare, M. W.; Resources, Nakitare, M. W.; Formal analysis, Agesa, W. N. and Tsimbasi, S. C.; Investigation, Agesa, W. N.; Data curation, Tsimbasi, S. C.; Writing—original draft preparation, Agesa, W. N. and Stella, M.; Writing—review and editing, Agesa, W. N. and Nakitare, M. W., and Stella, M.; Visualization, Tsimbasi, S. C.; Supervision, Nakitare, M. W. and Stella, M. All authors have read and agreed to the published version of the manuscript.

Conflicts of Interest

The authors declare no conflicts of interest regarding the publication of this paper.

References

[1] Li, F., Roccaforte, F., Greco, G., Fiorenza, P., La Via, F., Pérez-Tomas, A., *et al.* (2021) Status and Prospects of Cubic Silicon Carbide Power Electronics Device Technology. *Materials*, **14**, Article 5831. https://doi.org/10.3390/ma14195831

[2] Okumura, H. (2015) A Roadmap for Future Wide Bandgap Semiconductor Power Electronics. *MRS Bulletin*, **40**, 439-444. https://doi.org/10.1557/mrs.2015.97

[3] Kimoto, T. and Watanabe, H. (2020) Defect Engineering in SiC Technology for High-Voltage Power Devices. *Applied Physics Express*, **13**, Article 120101.

https://doi.org/10.35848/1882-0786/abc787

[4] Capan, I. (2025) Electrically Active Defects in 3C, 4H, and 6H Silicon Carbide Polytypes: A Review. *Crystals*, **15**, Article 255. https://doi.org/10.3390/cryst15030255

[5] Viewegh, N., Holloway, H., Biggerstaff, R., Herzog, J.B. and Stanley, C.M. (2026) Wide Bandgap Semiconductors for Power Electronics: Comparative Properties, Applications, and Reliability of GaN and SiC Devices. *Hardware*, **4**, Article 6. https://doi.org/10.3390/hardware4010006

[6] La Via, F., Severino, A., Anzalone, R., Bongiorno, C., Litrico, G., Mauceri, M., *et al.* (2018) From Thin Film to Bulk 3C-SiC Growth: Understanding the Mechanism of Defects Reduction. *Materials Science in Semiconductor Processing*, **78**, 57-68. https://doi.org/10.1016/j.mssp.2017.12.012

[7] Van Zeghbroeck, B.J. and Fardi, H. (2018) Comparison of 3C-SiC and 4H-SiC Power MOSFETs. *Materials Science Forum*, **924**, 774-777. https://doi.org/10.4028/www.scientific.net/msf.924.774

[8] La Via, F., Zimbone, M., Bongiorno, C., La Magna, A., Fisicaro, G., Deretzis, I., *et al.* (2021) New Approaches and Understandings in the Growth of Cubic Silicon Carbide. *Materials*, **14**, Article 5348. https://doi.org/10.3390/ma14185348

[9] Brzozowski, E., Kaminski, M., Taube, A., Sadowski, O., Krol, K. and Guziewicz, M. (2023) Carrier Trap Density Reduction at SiO_2/4H-Silicon Carbide Interface with Annealing Processes in Phosphoryl Chloride and Nitride Oxide Atmospheres. *Materials*, **16**, Article 4381. https://doi.org/10.3390/ma16124381

[10] Kim, K.Y., Noh, J.S., Yoon, T.Y. and Kim, J.H. (2021) Improvement in Turn-Off Loss of the Super Junction IGBT with Separated N-Buffer Layers. *Micromachines*, **12**, Article 1422. https://doi.org/10.3390/mi12111422

[11] Wang, J., Xie, X., Zhong, G., Chen, X., Yang, X., Sun, L., *et al.* (2026) Toward Low-Resistivity P-Type Sic Single Crystals: Controlling Doping and Defects. *Progress in Crystal Growth and Characterization of Materials*, **72**, Article 100708. https://doi.org/10.1016/j.pcrysgrow.2026.100708

[12] Calabretta, C., Scuderi, V., Anzalone, R., Mauceri, M., Crippa, D., Cannizzaro, A., *et al.* (2021) Effect of Nitrogen and Aluminum Doping on 3C-SiC Heteroepitaxial Layers Grown on 4° Off-Axis Si (100). *Materials*, **14**, Article 4400. https://doi.org/10.3390/ma14164400

[13] Kimoto, T. (2015) Material Science and Device Physics in Sic Technology for High-Voltage Power Devices. *Japanese Journal of Applied Physics*, **54**, Article 040103. https://doi.org/10.7567/jjap.54.040103

[14] Sun, L., Peng, B. and Zhang, W. (2025) First-Principles Study on the Stability, Electronic Structure, and Optical Properties of Neutral Phosphorus-Related Point Defects in 4H-SiC. *AIP Advances*, **15**, Article 045220. https://doi.org/10.1063/5.0266074

[15] Schöler, M., Lederer, M.W., Schuh, P. and Wellmann, P.J. (2020) Intentional Incorporation and Tailoring of Point Defects during Sublimation Growth of Cubic Silicon Carbide by Variation of Process Parameters. *Physica Status Solidi* (*B*), **257**, Article 1900286. https://doi.org/10.1002/pssb.201900286

[16] Wu, J., Xu, Z., Liu, L., Hartmaier, A., Rommel, M., Nordlund, K., *et al.* (2021) MD Simulation Study on Defect Evolution and Doping Efficiency of P-Type Doping of 3C-SiC by Al Ion Implantation with Subsequent Annealing. *Journal of Materials Chemistry C*, **9**, 2258-2275. https://doi.org/10.1039/d0tc05374k

[17] Bathen, M.E., Lew, C.T.K., Woerle, J., Dorfer, C., Grossner, U., Castelletto, S., *et al.*

(2022) Characterization Methods for Defects and Devices in Silicon Carbide. *Journal of Applied Physics*, **131**, Article 140903. https://doi.org/10.1063/5.0077299

[18] Ramakers, S., Marusczyk, A., Amsler, M., Eckl, T., Mrovec, M., Hammerschmidt, T., *et al.* (2022) Effects of Thermal, Elastic, and Surface Properties on the Stability of SiC Polytypes. *Physical Review B*, **106**, Article 075201. https://doi.org/10.1103/physrevb.106.075201

[19] Hasan, S., San, S., Baral, K., Li, N., Rulis, P. and Ching, W. (2022) First-Principles Calculations of Thermoelectric Transport Properties of Quaternary and Ternary Bulk Chalcogenide Crystals. *Materials*, **15**, Article 2843. https://doi.org/10.3390/ma15082843

[20] Madsen, G.K.H. and Singh, D.J. (2006) BoltzTraP. A Code for Calculating Band-Structure Dependent Quantities. *Computer Physics Communications*, **175**, 67-71. https://doi.org/10.1016/j.cpc.2006.03.007

[21] Tan, C.S. (2023) Electrical Conductivity Improvement of Point Defects in 4H-SiC. *Crystal Growth & Design*, **23**, 6250-6257. https://doi.org/10.1021/acs.cgd.3c00611

[22] Giannozzi, P., Baroni, S., Bonini, N., Calandra, M., Car, R., Cavazzoni, C., *et al.* (2009) QUANTUM ESPRESSO: A Modular and Open-Source Software Project for Quantum Simulations of Materials. *Journal of Physics*: *Condensed Matter*, **21**, Article 395502. https://doi.org/10.1088/0953-8984/21/39/395502

[23] Kresse, G. and Joubert, D. (1999) From Ultrasoft Pseudopotentials to the Projector Augmented-Wave Method. *Physical Review B*, **59**, 1758-1775. https://doi.org/10.1103/physrevb.59.1758

[24] Gražulis, S., Chateigner, D., Downs, R.T., Yokochi, A.F.T., Quirós, M., Lutterotti, L., *et al.* (2009) Crystallography Open Database—An Open-Access Collection of Crystal Structures. *Journal of Applied Crystallography*, **42**, 726-729. https://doi.org/10.1107/s0021889809016690

[25] Giannozzi, P., Andreussi, O., Brumme, T., Bunau, O., Buongiorno Nardelli, M., Calandra, M., *et al.* (2017) Advanced Capabilities for Materials Modelling with Quantum ESPRESSO. *Journal of Physics: Condensed Matter*, **29**, Article 465901. https://doi.org/10.1088/1361-648x/aa8f79

[26] Monkhorst, H.J. and Pack, J.D. (1976) Special Points for Brillouin-Zone Integrations. *Physical Review B*, **13**, 5188-5192. https://doi.org/10.1103/physrevb.13.5188

[27] Methfessel, M. and Paxton, A.T. (1989) High-Precision Sampling for Brillouin-Zone Integration in Metals. *Physical Review B*, **40**, 3616-3621. https://doi.org/10.1103/physrevb.40.3616

[28] Virtanen, P., Gommers, R., Oliphant, T.E., Haberland, M., Reddy, T., Cournapeau, D., *et al.* (2020) SciPy 1.0: Fundamental Algorithms for Scientific Computing in Python. *Nature Methods*, **17**, 352. https://doi.org/10.1038/s41592-020-0772-5

[29] Fritsch, F.N. and Carlson, R.E. (1980) Monotone Piecewise Cubic Interpolation. *SIAM Journal on Numerical Analysis*, **17**, 238-246. https://doi.org/10.1137/0717021

[30] Jiang, S., Li, Y., Chen, Z., Zhu, W., Wu, Q., He, H., *et al.* (2022) The Effects of Defects on the Defect Formation Energy, Electronic Band Structure, and Electron Mobility in 4H-SiC. *AIP Advances*, **12**, Article 065311. https://doi.org/10.1063/5.0095061

[31] Fan, T., Liu, W., Ruan, Z., Cao, Y., Ye, T., Liu, J., *et al.* (2022) First-Principles Investigation of Effects of Defects on the Physical Properties of 3C-SiC under High Temperatures and Pressures. *Journal of Materials Research and Technology*, **20**, 3633-3645. https://doi.org/10.1016/j.jmrt.2022.08.017

[32] Zhang, Y., Jiang, S., Li, Y., Chen, C., Chen, Z. and Wang, X. (2024) The Influence of

Point Defects on the Electronic Structures and Optical Properties of 3C-SiC. *AIP Advances*, **14**, Article 055009. https://doi.org/10.1063/5.0205402

[33] Qian, T.J. and Yang, J.H. (2025) First-Principles Studies of Nitrogen Doping in 4H-SiC. *Journal of Applied Physics*, **137**, Article 215701. https://doi.org/10.1063/5.0257680

[34] Bouzid, A. and Pasquarello, A. (2017) Identification of Semiconductor Defects through Constant-Fermi-Level *Ab Initio* Molecular Dynamics: Application to GaAs. *Physical Review Applied*, **8**, Article 014010. https://doi.org/10.1103/physrevapplied.8.014010

[35] Muchiri, P., Kipronoh, K., Makau, N. and Amolo, G. (2018) *Ab Initio* Calculation of Structural and Electronic Properties of 3C-Silicon Carbide: Density Functional Theory Calculations. https://ir.kabarak.ac.ke/items/63483321-e232-4b13-b400-9e275913b96d

[36] Jiang, S., Hu, C., Wang, D., Zhong, Y. and Tang, C. (2023) Electronic, Optical, Mechanical, and Electronic Transport Properties of $SrCu_2O_2$: A First-Principles Study. *Materials*, **16**, Article 1829. https://doi.org/10.3390/ma16051829

[37] Togo, A., Chaput, L., Tadano, T. and Tanaka, I. (2023) Implementation Strategies in Phonopy and Phono3py. *Journal of Physics: Condensed Matter*, **35**, Article 353001. https://doi.org/10.1088/1361-648x/acd831

[38] Kang, S., Fan, S. and Hu, G. (2025) Great Reduction of the Hole Effective Mass in Wide Bandgap Semiconductors by Highly Mismatched Alloying. *Physical Chemistry Chemical Physics*, **27**, 5694-5700. https://doi.org/10.1039/d4cp03957b

[39] Dou, Y.K., Qi, X., Jin, H.B., Cao, M.S., Zahid, U. and Hou, Z.L. (2012) First Principle Study of the Electronic Properties of 3C-SiC Doped with Different Amounts of Ni. *Chinese Physics Letters*, **29**, Article 077701. https://doi.org/10.1088/0256-307x/29/7/077701

[40] Liu, Z., Yang, X., He, X. and Sun, Y. (2026) Computational Screening of Bonding-Controlled Electronic Structures in One-Dimensional Cu/Ag-Based Hybrid Semiconductors. *Materials*, **19**, Article 1393. https://doi.org/10.3390/ma19071393

[41] Huang, Z., Guo, X., Yang, Y., Sheng, D., Li, H., Wang, Y., *et al.* (2025) Thermal Conductivity of Cubic Silicon Carbide Single Crystals Heavily Doped by Nitrogen. *Journal of Applied Physics*, **138**, Article 215104. https://doi.org/10.1063/5.0297824

[42] Kinaci, A., Kado, M., Rosenmann, D., Ling, C., Zhu, G., Banerjee, D., *et al.* (2015) Electronic Transport in VO_2—Experimentally Calibrated Boltzmann Transport Modeling. *Applied Physics Letters*, **107**, Article 262108. https://doi.org/10.1063/1.4938555

[43] Meng, F., Ma, J., He, J. and Li, W. (2019) Phonon-Limited Carrier Mobility and Temperature-Dependent Scattering Mechanism of 3C-SiC from First Principles. *Physical Review B*, **99**, Article 045201. https://doi.org/10.1103/physrevb.99.045201

[44] Li, Z., Graziosi, P. and Neophytou, N. (2022) Electron and Hole Mobility of SnO_2 from Full-Band Electron-Phonon and Ionized Impurity Scattering Computations. *Crystals*, **12**, Article 1591. https://doi.org/10.3390/cryst12111591

[45] Fardi, H. (2025) Study of 3C-SiC Power MOSFETs. *Micromachines*, **16**, Article 1406. https://doi.org/10.3390/mi16121406

[46] Tobehn-Steinhäuser, I., Reiche, M., Schmelz, M., Stolz, R., Fröhlich, T. and Ortlepp, T. (2021) Carrier Mobility in Semiconductors at Very Low Temperatures. *The 8th International Symposium on Sensor Science*, Dresden, 16-17 May 2021, 2-3.

[47] Jennings, J.R. (2025) Carrier Transport and Recombination in Sensitized Nanostruc-

tured TiO_2. In: Pan, J.H., Lee, W.I. and Bahnemann, D.W., *Nanostructured TiO_2*, Wiley, 159-184.

[48] Alkauskas, A., Yan, Q.M. and Van de Walle, C.G. (2014) First-Principles Theory of Nonradiative Carrier Capture via Multiphonon Emission. *Physical Review B*, **90**, Article 075202. https://doi.org/10.1103/physrevb.90.075202